Ocean Engineering 215 (2020) 107857

Contents lists available at ScienceDirect

Ocean Engineering

journal homepage: www.elsevier.com/locate/oceaneng

A new CFD method for determination of translational added mass coefficients of an underwater vehicle

Ehsan Javanmard [a,*], Shahriar Mansoorzadeh [b], Javad A. Mehr [c]

[a] Department of Mechanical Engineering, Isfahan University of Technology, Isfahan, Iran
[b] Subsea Science & Technology Center, Isfahan University of Technology, Isfahan, Iran
[c] National Centre for Maritime Engineering and Hydrodynamics, Australian Maritime College, University of Tasmania, Launceston, Tasmania, Australia

ARTICLE INFO

Keywords:
Underwater vehicle
Added mass coefficients
CFD
RANS simulations

ABSTRACT

In this paper, a new computational fluid dynamics approach is suggested to calculate translational longitudinal and transverse added mass coefficients of an underwater vehicle. In this method, the linear accelerated motion of the underwater vehicle is numerically simulated based on unsteady Reynolds Averaged Navier-Stokes equations using ANSYS CFX software. Velocity and acceleration related forces are extracted from the simulation results, from which the added mass coefficients are extracted. To validate obtained results, initially, the drag and added mass coefficients of an ellipsoid are calculated using the present method and compared with the available corresponding analytical and experimental results. Moreover, an acceleration sensitivity study was performed, indicating that calculated added mass coefficients were acceleration independent. The obtained results from the suggested numerical method agreed well with those obtained from the analytical and experimental methods, indicating that the present CFD method can be used to obtain the added mass coefficients of more complicated geometries, including the underwater vehicle used in this study. The proposed CFD method is not complicated and time-consuming. It can be used as a reliable and inexpensive method to extract translational added mass coefficients of underwater vehicles instead of expensive experimental methods or other CFD methods simulating oscillatory motions.

1. Introduction

Added mass coefficients are a key part of the hydrodynamic coefficients of an underwater vehicle, representing the dynamic behavior of the vehicle during accelerating motion. In other words, the added mass is an additional hydrodynamic reaction force generated by the surrounding water when the underwater vehicle accelerates (Prestero, 2001). Estimating inaccurate added mass coefficients results in inefficient dynamic model, and consequently, affects manoeuvrability of the vehicle.

In the hydrodynamic analysis of an underwater vehicle, two reference frames, namely, body-fixed and earth-fixed reference frames are introduced. The body-fixed reference frame is a moving coordinate frame fixed to the vehicle. Linear and angular velocities are given relative to this frame. In the earth-fixed reference frame, on the other hand, the position and orientation of the vehicle are given relative to a fixed origin. The origin of the earth-fixed frame is a specific point in space, while the origin of the body-fixed frame is the center of buoyancy of the vehicle. The body-fixed and earth-fixed coordinate frames for an underwater vehicle with six Degrees of Freedom (DOF) motion along with applied hydrodynamic loads are shown in Fig. 1.

The dynamics of an Underwater Vehicle motion is analyzed using mathematical models known as the dynamic model. The dynamic model covers all hydrodynamic forces and moments applied to the underwater vehicle. These hydrodynamic loads are not usually constant in time. They are a function of the velocity, acceleration, and the shape of the vehicle. Therefore, they are expressed as hydrodynamic coefficients multiplied by linear and angular velocities and accelerations. Linearized equations of the motion, including hydrodynamic loads applied to the vehicle with 6 DOF, are shown in Equations (1)–(6). These equations represent the dynamic model of the vehicle using a hydrodynamic

Abbreviations: ASE, Analytical & Semi-Empirical; BEM, Boundary Element Method; CFD, Computational Fluid Dynamics; CMD, Conning Motion Device; DOF, Degree of Freedom; EMM, Equivalent Ellipsoid Method; EFD, Experimental Fluid Dynamics; FVM, Finite Volume Method; GCI, Grid Convergence Index; PM, Panel Method; PMM, Planar Motion Mechanism; RA, Rotating Arm; RANS, Reynolds-Averaged Navier-Stokes; SST, Shear Stress Transport; ST, Strip Theory.

* Corresponding author.
E-mail address: javanmard.ehsan1363@gmail.com (E. Javanmard).

https://doi.org/10.1016/j.oceaneng.2020.107857
Received 9 May 2020; Received in revised form 23 July 2020; Accepted 25 July 2020
Available online 14 August 2020

Nomenclature

A	Projected area (m^2)
a	Acceleration (m s^{-2})
a, b, c	Ellipsoid specifications
CD	Drag force coefficient
CDA	Drag coefficient based on Projected area (A)
CD∀	Drag coefficient based on volume (∀2/3)
Cf	Skin-friction coefficient
CP	Pressure coefficient
CPM	Pressure coefficient caused by acceleration
D	Drag force (N)
e	Eccentricity
ea21	Approximate relative error
eext21	Extrapolated relative error
Fst	Applied force caused by velocity (N)
Ftr	Applied force caused by velocity and acceleration (N)
fi	External body force in *i*-direction (N)
hi	Grid size of the ith grid (m)
K	Roll moment (N m)
k1, k2	Lamb's *k*-factors
l	Reference length (m)
M	Pitch moment (N m)
ma	Added mass (Kg)
N	Yaw moment (N m)
P	Pressure (N m^{-2})
Pref	Reference pressure
pa	Apparent order
p	Roll angular velocity (rad s^{-1})
q	Pitch angular velocity (rad s^{-1})
r	Yaw angular velocity (rad s^{-1})
ro	Position vector of the vehicle (m)
rij	Grid refinement factor of jth grid toward ith grid
Re	Reynolds
Rel	Reynolds based on length
Uref	Reference velocity
Ui	Fluid velocity in *i*-direction (m s^{-1})
UiUj	Reynolds stresses
u	Surge velocity (m s^{-1})
V	Velocity (m s^{-1})
v	Sway velocity (m s^{-1})
w	Heave velocity (m s^{-1})
X	Surge force (N)
Y	Sway force (N)
Z	Heave force (N)
ρ	Density (kg m^{-3})
Δ	Standard deviation (%)
Δy	First layer thickness (m)
Δy+	Dimensionless first layer thickness
∅	Roll angle (degree)
θ	Pitch angle (degree)
ψ	Yaw angle (degree)
∅k	Key variable obtained from kth grid
∅ext21	Extrapolated value
∀	Volume (m^3)
λ	Fineness ratio
υ	Cinematic viscosity (m^2 s^{-1})

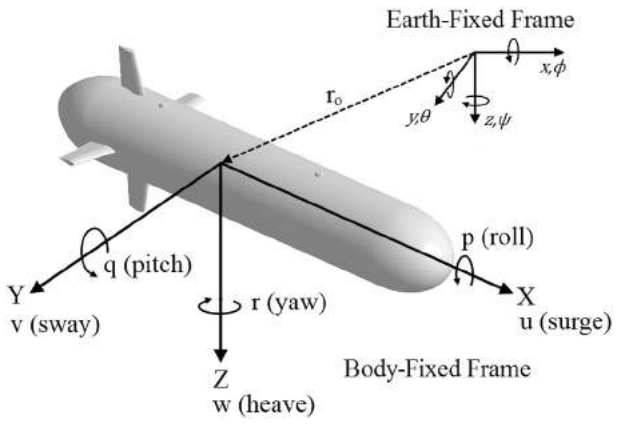

Fig. 1. Body and earth-fixed coordinate frames with hydrodynamic loads acting on the underwater vehicle.

derivatives concept. Determination of the hydrodynamic coefficients used in these equations is crucial stage of performing hydrodynamic analysis.

$$\sum X_{net} = X_u u + X_{\dot{u}}\dot{u} + X_q q \tag{1}$$

$$\sum Y_{net} = Y_v v + Y_r r + Y_{\dot{v}}\dot{v} + Y_{\dot{r}}\dot{r} + Y_{\delta_r}\delta_r \tag{2}$$

$$\sum Z_{net} = Z_w w + Z_q q + Z_{\dot{w}}\dot{w} + Z_{\dot{q}}\dot{q} + Z_{\delta_s}\delta_s \tag{3}$$

$$\sum K_{net} = K_P p + K_{\dot{P}}\dot{p} \tag{4}$$

$$\sum M_{net} = M_w w + M_q q + M_{\dot{w}}\dot{w} + M_{\dot{q}}\dot{q} + M_{\delta_S}\delta_S \tag{5}$$

$$\sum N_{net} = N_v v + N_r r + N_{\dot{v}}\dot{v} + N_{\dot{r}}\dot{r} + N_{\delta_r}\delta_r \tag{6}$$

Based on the type of the hydrodynamic loads applied to the underwater vehicle, the hydrodynamic coefficients in Equations (1)–(6) are divided into two sets of damping and added mass coefficients. When the underwater vehicle moves with a constant velocity, the drag and lift forces constitute the main resistance loads applied to the vehicle. These hydrodynamic loads, which are functions of the vehicle shape and the velocity, are known as damping loads. The corresponding hydrodynamic coefficients are known as damping coefficients.

Given the dynamic model in Equations (1)–(6), the coefficients X_u, X_q, Y_v, Y_r, Y_{δ_r}, Z_w, Z_q, Z_{δ_s}, K_P, M_w, M_q, M_{δ_s}, N_v, N_r and N_{δ_r} are damping coefficients of the underwater vehicle. Other hydrodynamic loads are applied to the vehicle when it changes its velocity or its motion direction. The value of these loads depends on angular and transitional accelerations or Coriolis effects. Therefore, hydrodynamic coefficients representing these loads are called as added mass coefficients. In Equations (1)–(6), these coefficients include $X_{\dot{u}}$, $Y_{\dot{v}}$, $Y_{\dot{r}}$, $Z_{\dot{w}}$, $Z_{\dot{q}}$, $K_{\dot{P}}$, $M_{\dot{w}}$, $M_{\dot{q}}$, $N_{\dot{v}}$and $N_{\dot{r}}$.

There are several methods used by researchers to predict the hydrodynamic coefficients of submersible vehicles. These methods include Analytical & Semi-Empirical (ASE), Experimental Fluid Dynamics (EFD), and Computational Fluid Dynamics (CFD). Peterson (1980), Humphreys (1981), Maeda and Tatsuta (1989), Nahon (1993), Jones and Clarke (2002), Geisbert (2007) and Isa et al. (2014) are among those researchers who used ASE methods to calculate the hydrodynamic coefficients. Regarding EFD methods, Gerfler (1967), Aage et al. (1994), Rhee et al. (2001), Ridley et al. (2003), Jagadeesh et al. (2009), Lee et al. (2011), Avila and Adamowski (2011), Avila et al. (2012), Javanmard (2013), Zhang and Zou (2013), Nakamura et al. (2013), Krishnankutty

(2014), Saeidinezhad et al. (2015), Kim et al. (2015a) and Park et al. (2017) used various experimental tools such as towing tank, Rotating Arm (RA), Conning Motion Device (CMD), and Planar Motion Mechanism (PMM) to estimate hydrodynamic coefficients. On the other hand, Hopkin and Den Hertog (1993), Nahon (1993), Bellevre et al. (2000), Cimbala (2003), Wu et al. (2005), Tyagi and Sen (2006), Phillips et al. (2007), Broglia et al. (2007), Hu et al. (2007), Barros et al. (2008), Sakamoto (2009), Tang et al. (2009), Jagadeesh and Murali (2010), Zhang et al. (2010), Phillips and Turnock (2010), Phillips et al. (2010), Mishra et al. (2011), Pan et al. (2012), Malik and Guang (2013), Zhang et al. (2013), Mansoorzadeh and Javanmard (2014), Leong et al. (2015), Kim et al. (2015a, 2015b), Liang et al. (2016), Shadlaghani and Mansoorzadeh (2016), Chen et al. (2017), Guo and Zou (2017), Pook et al. (2018), Javanmard and Mansoorzadeh (2019), and Go and Ahn (2019) used CFD to obtain hydrodynamics coefficients. Added mass coefficients, in particular, can be obtained using EFD, CFD, and ASE methods. In experimental methods, dynamic tests using RA and PMM are performed to apply the required motions and maneuvers to the vehicle on horizontal and vertical planes. Perturbed surge maneuver, pure sway, and pure yaw are among the oscillatory, and hence accelerating, motions that are generated by a PMM. These accelerated motions apply hydrodynamic loads to the vehicle that are measured and analyzed through performing a detailed Fourier analysis to calculate added mass coefficients. CFD includes two ways to estimate added mass coefficients of submersible vehicles. The first one is based on the assumption of the potential flow and includes Panel Method (PM) and Boundary Element Method (BEM). In practice, due to the viscosity of the fluid flow around the vehicle, this assumption decreases the accuracy of the obtained results. Sahin et al. (1993, 1997) and Lin and Liao (2011) used PM and BEM to estimate added mass coefficients of underwater vehicles. In a second way, commercial CFD software is applied to simulate dynamic tests performed by PMM and RM. In these simulations Reynolds Averaged Navier-Stokes (RANS) equations, including viscosity effect, are solved in a computational domain. Among researchers implementing CFD simulations to predict added mass coefficients, studies conducted by Phillips et al. (2007), Sakamoto (2009), Tang et al. (2009), Zhang et al. (2010), Javanmard (2013) and Kim et al. (2015b) are notable. Analytical methods, including Strip Theory (ST) and Equivalent Ellipsoid Method (EMM) only rely on the geometric specifications of the vehicle to calculate the added mass coefficients. The main principle in these methods is to find the velocity potential using boundary conditions and use it to determine pressure distribution around the vehicle based on Bernoulli's equation. Finally, obtained pressure distribution yields the hydrodynamic forces and moments applied on the vehicle. According to ST, a vehicle can be made up of a finite number of transversal two-dimensional slices, and the added mass of the whole vehicle is obtained by integration of the value of the slice over the length of the vehicle (Sen and Vinh, 2016). Korvin-Kroukovsky and Jacobs (1957) introduced the first formulation of the ST known as the Ordinary Strip Theory Method. This method, then, was developed by Tasai (1969) with Modified Strip Theory Method. Perstro (2001) and Ferreira et al. (2009) implemented ST to calculate added mass coefficients of underwater vehicles. In EMM, different parts of the vehicle are relatively assumed as equivalent ellipsoids with specified geometrical parameters. Using the analytical methods, the added mass coefficients of any specific ellipsoid can be obtained through solving Laplace equations for velocity potential. Integration of the all calculated added mass coefficients, for different parts of the vehicle, in a specific direction, yields the added mass coefficient of the whole vehicle in the desired direction. Lamb (1945), Fossen (1994), and Korotkin (2009) are the main references in this area. ASE method is only recommended for vehicles with simple geometry since their accuracy declines by increasing the complicacy of the vehicle's geometry. Therefore, this method requires adequate experimental data and cannot take the complicated shape of an underwater vehicle into full account (Pan et al., 2012; Go and Ahn, 2019). Additionally, the potential-based methods can predict the inertial hydrodynamic coefficients satisfactorily, but with the viscous terms neglected (Pan et al., 2012). Moreover, although EFD methods may be the most reliable way to obtain added mass coefficients, it is not only costly, due to requiring special facilities and equipment such as PMM to apply the accelerated motions to the vehicle, but also time-consuming. Furthermore, although applying CFD to simulate oscillatory motions applied by a PMM or RA eliminates the need for such equipment, there are still some ambiguities in CFD simulations of the oscillatory motions that need to be dealt with. Thus, it has been likely to use CFD as a supplementary method besides experimental tests.

Although there have been some studies on CFD simulations of accelerating underwater bodies with forwarding speed, conducted by Cimbala (2003) and Mishra et al. (2011), the majority of numerical investigations have been performed to obtain added mass coefficients of ocean vehicles through simulating of the oscillatory motions. The added mass has been previously predicted as a function of frequency and not of time, while for streamlined underwater accelerating vehicles with forwarding speed, added mass not only is time-dependent but also has a significant effect on the dynamic behavior of the vehicle. The goal of this paper is to propose a CFD method to calculate translational added mass coefficients of an axisymmetric underwater vehicle in both longitudinal and transverse directions. The proposed method includes CFD simulations of the linear accelerated motion of an academic underwater vehicle with forwarding speed based on Unsteady RANS equations using a Finite Volume Method (FVM). Comparing this method with other methods indicates that the current method is simple, relatively fast and quite accurate which can be used to obtain translational added mass coefficients of vehicles with complicated geometries. One of the advantages of this method is that an experimental test can be performed in a towing tank facility, with conditions similar to the proposed numerical method. The obtained results of both methods, then, can be compared.

The geometric model of the vehicle used for the current study is shown in Fig. 2. The main characteristics of the vehicle are listed in Table 1.

2. Methodology

To estimate translational longitudinal and transverse added mass coefficients of the vehicle using unsteady forward speed, CFD simulations of the accelerated flow around the vehicle in the x (longitudinal) and y (transverse) directions are required. In the present work, these accelerated motions are generated using two procedures discussed in detail in the following sections.

2.1. Procedure one

As can be seen in Fig. 3 (a), in this procedure, it is assumed that in a steady motion during the time period between $t = 0$ to $t = t_0$, the vehicle moves with a constant forward speed of V_0 inside the fluid domain. Then, at $t = t_0$, this motion is changed into an accelerated motion. As can be seen in Fig. 3 (b), at $0 \leq t < t_0$the applied force on the vehicle, named F_{st}, only includes drag force that is proportional to squared velocity. Therefore, in this period, F_{st} remains unchanged since the velocity is constant. However, at $t = t_0$ when the velocity profile changes to an

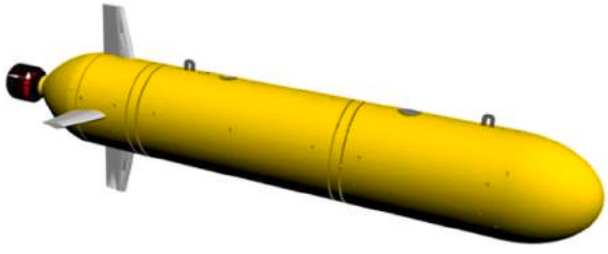

Fig. 2. Underwater Vehicle used for the current study.

Table 1
Main characteristics of the underwater vehicle.

Parameters	Description
Shape	Torpedo
Length (m)	1.45
Diameter (m)	0.23
Weight in the air (kg)	45
Depth of operation (m)	2
Time of operation (hr)	2.5
Fins profile	NACA0015
Horizontal velocity (Knot)	3

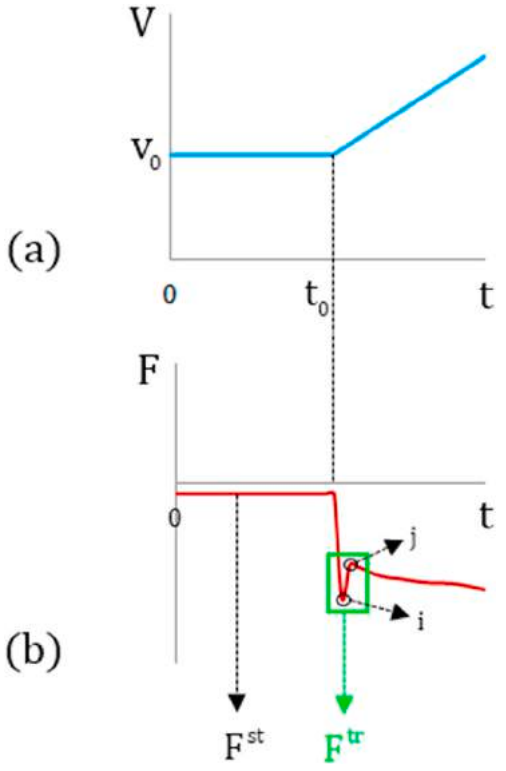

Fig. 3. Velocity profile at the inlet boundary (a) and applied force on the vehicle (b) in procedure one.

accelerated motion, the inertia force of the fluid is added to the drag force. Therefore, as accelerated motion begins, the dynamic pressures increases at the upstream while the effects of acceleration are not felt at the downstream. This temporal pressure difference increases the pressure drag locally and, in return, the applied force on the vehicle at the beginning of the acceleration (point i). As the accelerated flow expands on the whole computational domain, the initial local pressure difference starts to decrease, leading to a reduction in drag force. Then, in point j, accelerated flow is expanded thoroughly in the domain. This means that from point i to point j it takes a while for the accelerated flow to expand thoroughly over the fluid. This feature is known as history effect. Without this effect the applied force to the vehicle at $t = t_0$would be as illustrated in Fig. 4 (point k). According to Fig. 3, at $t = t_j$, applied force, named F_{tr}, consists of both drag force (F_{st}), which is of viscous origin and the hydrodynamic or inertia force of the fluid, which is proportional to the acceleration of the vehicle. $F_{tr}$is equal to $(\rho\forall + m_a)|a|$, where $\rho\forall$represents the mass of the displaced volume of the fluid occupied by

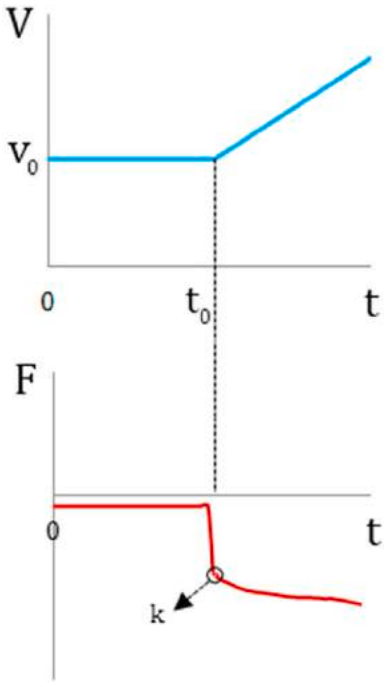

Fig. 4. Applied force on the vehicle without history effect in procedure one.

the vehicle, m_a is added mass of the vehicle in the intended direction and a is acceleration in the intended direction. Therefore, $m_a$can be obtained as follows:

$$m_a = \frac{|F^{tr} - F^{st}|}{|a|} - \rho\forall \tag{7}$$

The nominator of the first term in the right hand side of this equation is the applied force due to the acceleration of the vehicle. The estimate used in this method includes determination of the t_j. Therefore, this procedure entails an accurate estimate of the point j. Since applied force on the underwater vehicle has a notable variation around this point at a short period of time, accurate identification of the point is always featured with error, and obtained results include high inaccuracy. Thus, a second procedure is proposed, in which, estimating t_j is not required.

2.2. Procedure two

In the second procedure, the motion of the underwater vehicle is represented by a piecewise velocity function described as below:

$$V(t) = \begin{cases} V_0 & 0 < t \le t_0 \\ at + b_1 & t_0 \le t \le t_1 \\ V_1 & t_1 \le t \le t_2 \\ -at + b_2 & t_2 \le t \le t_3 \\ V_0 & t = t_3 \end{cases} \tag{8}$$

As can be seen in Fig. 5, at $t = t_3$decelerated motion of the vehicle reaches the initial velocity of V_0. At this time, the hydrodynamic force applied to the vehicle (point p) consists of the drag force of the vehicle at $V(t) = V_0$caused by the velocity effects as well as inertia force of the fluid surrounding the decelerating vehicle arisen as a result of added mass effect. Therefore, the difference of the hydrodynamic force at $t = t_3$and drag force at $t < t_0$represents fluid inertia force, which is equal to $(\rho\forall + m_a)|a|$.

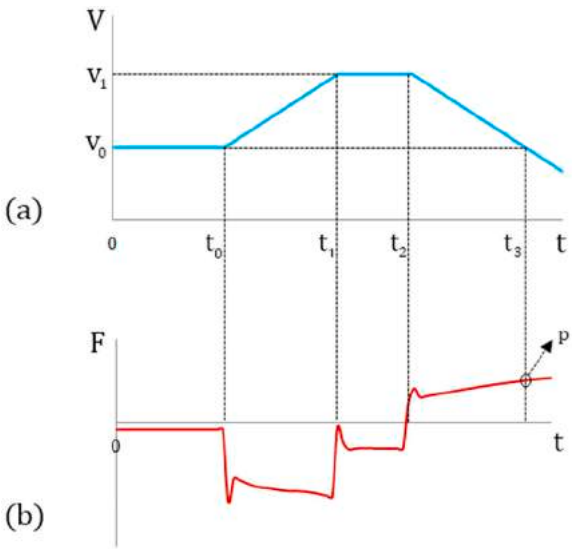

Fig. 5. Velocity profile at the inlet boundary (a) and applied forces on the vehicle (b) in procedure two.

$$\left|F_{t=t_3} - F_{t<t_0}\right| = (\rho\forall + m_a)|a| \tag{9}$$

$$m_a = \frac{\left|F_{t=t_3} - F_{t<t_0}\right|}{|a|} - \rho\forall \tag{10}$$

The main difference between two procedures is that at the second procedure, hydrodynamic force, including the acceleration effects (point p), is measured directly and doesn't need to any estimation. In contrast, the first procedure is based on the estimation of the hydrodynamic force after the history effect.

Therefore, in this paper the second procedure was used to calculate translational added mass coefficients of the underwater vehicle in both longitudinal and transverse directions. Comparing with previous CFD studies, this method neither ignores viscosity in pressure distribution computation nor needs to conduct complicated simulations such as PMM tests. The proposed method can simply simulate the accelerated motion of underwater vehicle moving with forward speed.

3. Validation

To validate the proposed CFD method, firstly, the obtained drag and added mass coefficients are compared with those of the analytical and experimental results. Secondly, the obtained results are investigated to be independent of the vehicle acceleration. To deal with these issues, translational longitudinal and transverse added mass coefficients of an ellipsoid are calculated using both the analytical method introduced by Lamb (1945) and the CFD method proposed in this study. Then, obtained results will be compared with each other as well as available experimental data collected by Lee at al. (2011). To this end, we consider a fully-submerged ellipsoid described in Equation (11) with specifications illustrated in Fig. 6.

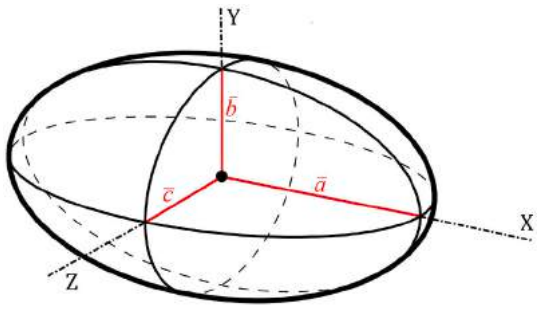

Fig. 6. Schematic of the ellipsoid used for validation study with $\bar{a} = 1(m)$ and $\bar{b} = \bar{c} = 0.2(m)$.

$$\frac{x^2}{\bar{a}^2} + \frac{y^2}{\bar{b}^2} + \frac{z^2}{\bar{c}^2} = 1 \tag{11}$$

3.1. Analytical method

3.1.1. Added mass coefficients

For an ellipsoid with $\bar{c} = \bar{b}$and $\bar{a} > \bar{b}$, Lamb (1945) introduced *k*-factors as:

$$k_1 = \frac{\alpha_0}{2 - \alpha_0}$$

$$k_2 = \frac{\beta_0}{2 - \beta_0} \tag{12}$$

Where $\alpha_0$and $\beta_0$are constants that are calculated based on the geometric specifications of an ellipsoid:

$$\alpha_0 = \frac{2(1-e^2)}{e^2}\left(\frac{1}{2}\ln\frac{1+e}{1-e} - e\right)$$

$$\beta_0 = \frac{1}{e^2} - \frac{1-e^2}{2e^2}\ln\frac{1+e}{1-e} \tag{13}$$

Where e is the eccentricity of the meridian elliptical section which is given as follows:

$$e^2 = 1 - \left(\frac{\bar{b}}{\bar{a}}\right)^2 \tag{14}$$

By defining *k*-factors, Lamb (1945) represented the following analytical formulation to calculate added mass derivatives of an ellipsoid in longitudinal and transverse directions:

$$\begin{aligned} X_{\dot{u}} &= -k_1 m \\ Y_{\dot{v}} &= Z_{\dot{w}} = -k_2 m \end{aligned} \tag{15}$$

Where, m represents the mass of the displaced volume of the fluid around the ellipsoid:

$$m = \rho\forall = \frac{4}{3}\rho\pi\bar{a}\bar{b}^2 \tag{16}$$

Given the geometric specifications of the ellipsoid in Fig. 6 and Equations (12)–(14), Lamb's *k*-factors can be calculated as

$$k_1 = 0.057859$$

$$k_2 = 0.897798 \tag{17}$$

Using calculated Lamb's *k*-factors and Equations (15-16), added mass coefficients of the ellipsoid in longitudinal and transverse directions can be obtained as follows:

$$X_{\dot{u}} = -9.682(kg)$$

$$Y_{\dot{v}} = Z_{\dot{w}} = -150.23(kg) \tag{18}$$

3.1.2. Drag coefficient

Hoerner (1965) offered an empirically derived formula to calculate the drag coefficient of streamlined bodies like ellipsoids as follows:

$$C_D = C_f\left(4\lambda^{(1/3)} + 6\lambda^{(-7/6)} + 24\lambda^{(-8/3)}\right) \tag{19}$$

Whereλ is fineness ratio ($\lambda = \frac{\bar{a}}{\bar{b}}$), and $C_f$is the skin-friction coefficient of an equivalent flat plate, which is a function of the Reynolds number as bellow:

Table 2
Drag coefficients of the ellipsoid in longitudinal mode.

V(m.s^{-1})	Re	C_f	C_D
1.5	2988048	0.00375	0.03032
3	5976096	0.00334	0.027

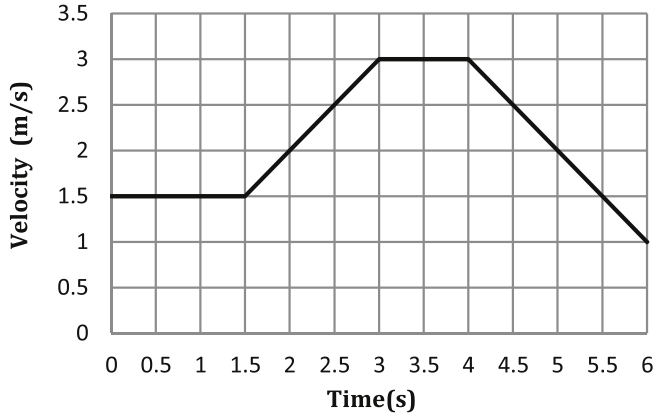

Fig. 7. Velocity profile used to simulate the accelerated motion of the ellipsoid in longitudinal and transverse directions.

$$C_f = \frac{0.455}{(\log_{10} Re)^{2.58}} = \frac{0.045}{Re^{(1/6)}}$$

$$Re = \frac{VL}{\upsilon} \tag{20}$$

Where $L = 2\bar{a}$and $\upsilon$is the kinematic viscosity of the water. Therefore, the drag coefficient of the proposed ellipsoid in longitudinal mode is obtained in two different velocities, as indicated in Table 2:

3.2. CFD method (procedure two)

Now, added mass coefficients of the ellipsoid in longitudinal ($X_{\dot{u}}$) and transverse ($Y_{\dot{v}}$) directions are extracted using the proposed CFD method. As noted, to calculate translational longitudinal and transverse added mass coefficients of a vehicle accelerated motion of the vehicle in the proposed direction should be simulated. Therefore, the piecewise velocity profile expressed in Equation (21) and shown in Fig. 7, was used to simulate the accelerated motions of the ellipsoid in longitudinal and transverse directions. ANSYS CFX commercial code was applied to carry out all simulations, including URANS computations based on an FVM. Moreover, ICEM CFD software was used to generate a structured mesh in computational domains. Fig. 8 illustrates a cut plan on the computational grid generated to simulate the accelerated motion of the ellipsoid in a longitudinal direction. More details of the numerical simulation are given in section 4. Figs. 9 and 10 show applied hydrodynamic forces on the ellipsoid in longitudinal and transverse accelerated motions, respectively.

$$V(t) = \begin{cases} 1.5 & 0 < t \le 1.5 \\ t & 1.5 \le t \le 3 \\ 3 & 3 \le t \le 4 - (t-4) + 3 \quad 4 \le t \le 6 \end{cases} \tag{21}$$

Using Figs. 9 and 10, and Equation (10) longitudinal and transverse added mass coefficients of the ellipsoid are obtained as follows:

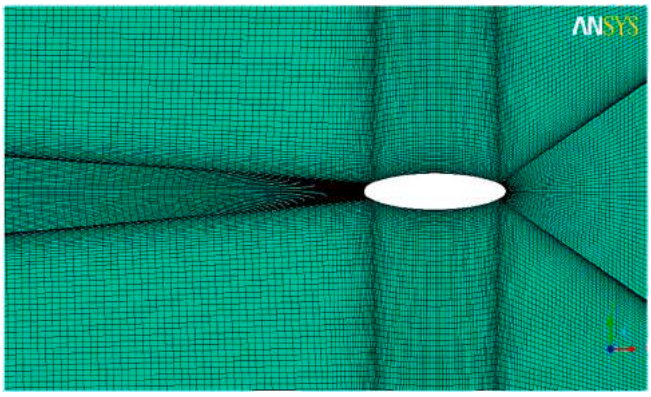

Fig. 8. Structured mesh on a cut plan around the ellipsoid used for CFD analysis in the longitudinal direction.

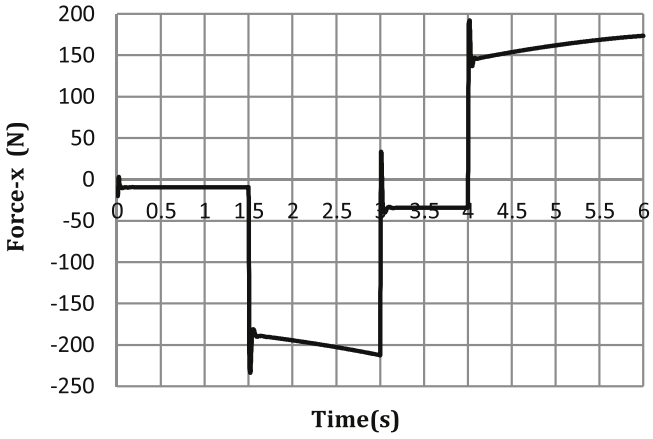

Fig. 9. Variation of the applied force on the ellipsoid in the longitudinal direction.

$$X_{\dot{u}} = \frac{|F_{t=5.5} - F_{t=1.5}|}{|\dot{u}|} - \rho\forall = 10.04\ (kg) \tag{22}$$

$$Y_{\dot{v}} = \frac{|F_{t=5.5} - F_{t=1.5}|}{|\dot{v}|} - \rho\forall = 143.48\ (kg) \tag{23}$$

Where. $a = |\dot{u}| = |\dot{v}| = 1(m.s^{-2})$

Table 3, compares obtained longitudinal and transverse added mass coefficients of the ellipsoid at $|a| = 1$ (m s^{-2}) using analytical and numerical methods. As indicated in this table, numerical results agreed well with those of the analytical method. Lee et al. (2011) obtained transverse added mass coefficient ($Y_{\dot{v}}$)of an ellipsoid with the same specifications using PMM producing oscillating pure sway motion. Experimental data, then, were compared with CFD results achieved by performing a numerical simulation of oscillating pure sway motion. Table 4, compares the transverse added mass coefficient of the ellipsoid obtained with the current CFD method with numerical and experimental results calculated by Lee et al. (2011). As indicated in Table 4, there is a discrepancy of 7.7% between numerical and experimental results obtained by Lee et al. (2011). Moreover, his numerical and experimental results have discrepancies of 15.84% and 9.38%, respectively, with transverse added mass coefficient obtained with analytical method,

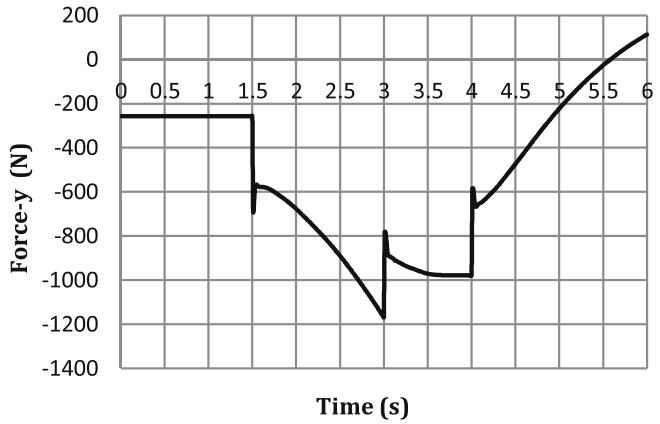

Fig. 10. Variation of the applied force on the ellipsoid in the transverse direction.

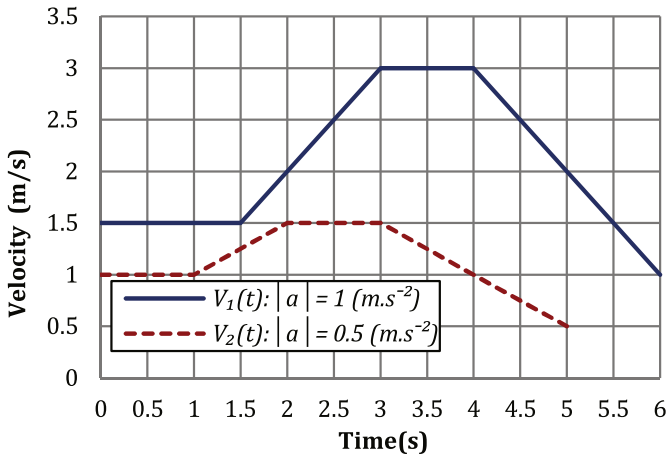

Fig. 11. Velocity profiles used for acceleration independent study.

Table 3
Longitudinal and transverse added mass coefficients of the ellipsoid obtained with analytical and numerical methods.

Hydrodynamic Coefficient	CFD Present	Analytical	$\|a\|$(m.s^{-2})	$\|\Delta\|$(%)
$X_{\dot{u}}$(kg)	10.04	9.682	1	3.57
$Y_{\dot{v}}$(kg)	143.48	150.23	1	4.70

Table 4
Comparison of transverse added mass coefficients of the ellipsoid.

Hydrodynamic Coefficient	EFD Lee et al. (2011)	CFD Lee et al. (2011)	CFD Present	Analytical
$Y_{\dot{v}}$(kg)	178.50	165.78	143.48	150.23

whereas, according to Table 3, current CFD method has only a difference of 4.7% with the analytical method in predicting transverse added mass coefficient of the ellipsoid. This reveals that to predict translational added mass coefficients of a vehicle in longitudinal and transverse directions, numerical methods where the accelerated motion of the vehicle is simulated by considering forward speed problem give more acceptable results than numerical methods simulating oscillating motions.

According to Fig. 9, drag force applied on the ellipsoid in longitudinal mode at $V = 1.5$ (m s^{-1}) and $V = 3$ (m s^{-1}) is 9.575 (N) and 34.22 (N) respectively. Thus, the drag coefficient of the ellipsoid in longitudinal mode can be calculated using an empirically derived formula given by Hoerner (1965) as bellow:

$$C_D^{\forall} = \frac{D}{\frac{1}{2}\rho V^2 \forall^{(2/3)}} \tag{24}$$

Where, $D$is drag force and $\forall$is the volume of the ellipsoid. Given Equation (24), the drag coefficient of the ellipsoid in longitudinal mode at two velocities can be calculated using the current CFD method. Table 5, compares longitudinal drag coefficients of the ellipsoid obtained with analytical and current CFD methods.

Table 5
Longitudinal drag coefficients of the ellipsoid at different velocities.

Hydrodynamic Coefficient	V(m.s^{-1})	CFD Present	Analytical	$\|\Delta\|$(%)
$C_D^{\forall}$	1.5	0.02803	0.03032	8.2
	3	0.02505	0.027	7.8

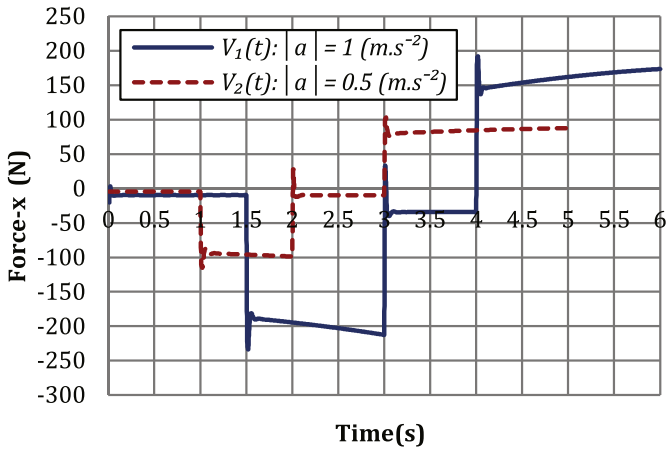

Fig. 12. Variation of the applied forces on the accelerated ellipsoid in the longitudinal direction at different velocity profiles.

3.3. Acceleration independent study

As noted, the results of the proposed CFD method should be independent of the acceleration of the vehicle. It is necessary, therefore, to examine this criterion. To this purpose, two piecewise velocity profiles expressed in Equations (25) and (26), and shown in Fig. 11, were used to simulate the accelerated motions of the ellipsoid at two different accelerations, $|a| = 1$ (m s^{-2}) & $|a| = 0.5$ (m s^{-2}), in the longitudinal direction to calculate $X_{\dot{u}}$. Applied hydrodynamic forces on the ellipsoid in longitudinal accelerated motions are shown in Fig. 12.

$$V_1(t) = \begin{cases} 1.5 & 0 < t \le 1.5 \\ t & 1.5 \le t \le 3 \\ 3 & 3 \le t \le 4 \\ -(t-4)+3 & 4 \le t \le 6 \end{cases} \tag{25}$$

$$V_2(t) = \begin{cases} 1 & 0 < t \le 1 \\ 0.5t + 0.5 & 1 \le t \le 2 \\ 1.5 & 2 \le t \le 3 \\ -0.5(t-3)+1.5 & 3 \le t \le 5 \end{cases} \tag{26}$$

Using Fig. 12 and Equation (10), longitudinal added mass coefficients of the ellipsoid at two velocity profile are obtained as follows:

$$\{X_{\dot{u}}\}_{|a|=1} = \frac{|F_{t=5.5} - F_{t=1.5}|}{|a|} - \rho\forall = 10.04\ (kg) \tag{27}$$

$$\{X_{\dot{u}}\}_{|a|=0.5} = \frac{|F_{t=4} - F_{t=1}|}{|a|} - \rho\forall = 10.25\ (kg) \tag{28}$$

As can be seen, there is a difference of 2.05% between the obtained results at different accelerations. This means that obtained numerical results with the proposed CFD method are acceleration independent. Given the validation, the proposed CFD method has the required accuracy to extracting translational added mass coefficients. Therefore, the proposed method was used to calculate translational longitudinal and transverse added mass coefficients of the underwater vehicle.

4. CFD simulation

ANSYS CFX commercial CFD software was applied to carry out all CFD simulations in this study. The software uses a unique finite volume approach to discretizing Navier-Stokes equations. Based on a vertex-centered finite volume scheme, ANSYS CFX solver satisfies strict global conservation by enforcing local conservation over control volumes that are constructed around each mesh vertex or node (www.ansys.com). CFD simulation procedure consists of governing equations, generating computational domain and computational grid, setting adequate boundary conditions, mesh independence study and verification study. All these steps are fully described below.

4.1. Governing equations

Incompressible RANS equations are the governing equations of the CFD simulations and consist of the continuity and momentum equations expressed as below (WHITE, 1985).

$$\frac{\partial \overline{U}_i}{\partial x_i}=0 \tag{29}$$

$$\frac{\partial \overline{U}_i}{\partial t}+\frac{\partial \overline{U_i U_j}}{\partial x_j}=-\frac{1}{\rho}\frac{\partial P}{\partial x_i}+\frac{\partial}{\partial x_j}\left\{v\left(\frac{\partial \overline{U}_i}{\partial x_j}+\frac{\partial \overline{U}_j}{\partial x_i}\right)\right\}-\frac{\partial \overline{U_i' U_j'}}{\partial x_j}+f_i \tag{30}$$

In these equations, $\overline{U}_i$and $f_i$refer to fluid velocity and external body force in i-direction, respectively. $P$and ρrefer to the fluid pressure and density, respectively. $v$is the total viscosity of the flow consisting of laminar and turbulent viscosity. The Shear Stress Transport (SST) turbulence model was employed to estimate the increased levels of stress within the boundary layer, termed the Reynolds stresses, $\overline{U_i' U_j'}$, and predict the turbulent viscosity. The SST turbulence model is a two-zone turbulence model blending a variant of $k-\omega$model with a $k-\varepsilon$in the outer boundary layer and far from the wall. Moreover, it is known as a reliable turbulence model to simulate flow separation caused by the adverse pressure gradient in the wake region of the moving bodies (Menter, 1994; Wilcox, 2006).

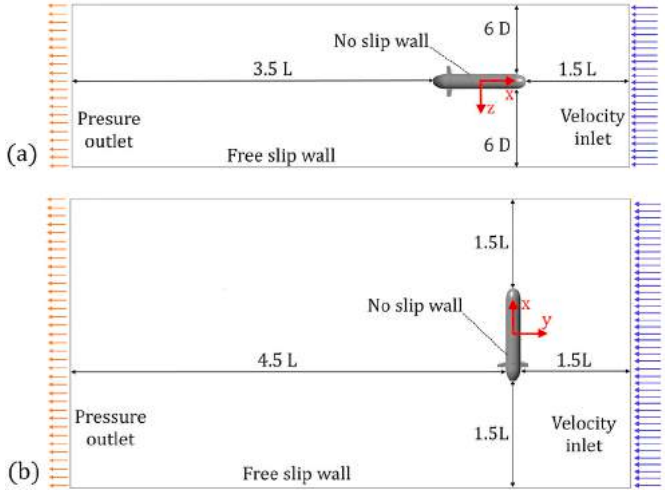

Fig. 13. Computational domains with specified boundary conditions: longitudinal accelerated motion mode (a); transverse accelerated motion mode (b).

4.2. Domain & mesh generation and boundary conditions

As shown in Fig. 13, the computational domains were generated as fixed cuboids in space surrounding a full-scale of the proposed underwater vehicle. The accelerated motion of the vehicle is represented by applying relative velocity profiles at the inlet boundary. As can be seen, the inlet boundary condition was located at 1.5L upstream of the vehicle with inlet velocity profile $U_{inlet}=(u(t),\,0,\,0)$for longitudinal accelerated motion and $U_{inlet}=(0,\,v(t),\,0)$for the transverse accelerated motion of the vehicle. $u(t)$and $v(t)$are described in Equations (31) and (32), respectively. An outlet boundary condition with zero relative pressure was applied at 3.5L downstream of the vehicle in longitudinal mode, Figs. 13(a), and 4.5L downstream of the vehicle in transverse mode, Fig. 13(b). Free-slip wall boundary condition was used for the sidewalls, located 6D and 1.5L away from the vehicle in longitudinal and transverse accelerated motions, respectively. No slip boundary condition was applied to the vehicle.

$$u(t)=\begin{cases}1.5 & 0<t\le 1.5\\ t & 1.5\le t\le 3\\ 3 & 3\le t\le 4-(t-4)+3 \qquad 4\le t\le 6\end{cases} \tag{31}$$

$$v(t)=\begin{cases}1 & 0<t\le 1\\ 0.5t+0.5 & 1\le t\le 2\\ 1.5 & 2\le t\le 3-0.5(t-3)+1.5 \qquad 3\le t\le 5\end{cases} \tag{32}$$

ANSYS ICEM CFD was applied to generate an unstructured mesh in computational domains. Since Low-Re turbulent models like SST aim to resolve the laminar sub-layer region ($y^+<5$) where viscous effects are dominant, an appropriate mesh resolution is required. Therefore, the average y$^+$value was set to be close to 1 to ensure that laminar sub-layer is fully resolved. To estimate the first prismatic layer thickness base on a specified value of y$^+$, an empirical equation expressed as $\Delta y=l\Delta y^+\sqrt{80}\,Re_l^{-13/14}$is recommended (ANSYS, 2009) where, l is the reference length equal to the length of the vehicle. Therefore, using $y^+=1$and the velocity of 1.5 m s^{-1}, the first layer thickness was about 0.017 mm. For all equations, high resolution and second-order backward Euler were used as discretization schemes for advection and transient terms, respectively. Using a time step of 0.012(s) resulted in a Courant number less than 1 and achieving the convergence criterion of 1e-5 in 4 internal iterations. All simulations were carried out on a desktop computer with 8-cores Xeon processors and 32 GB internal memory in double-precision and parallel mode.

Table 6
Grid characteristics used for mesh independence study and obtained results in longitudinal and transverse motion modes (*M means million, i.e.10^6).

Mode of the Motion	Longitudinal Motion Mode			Transverse Motion Mode		
Mesh Configuration	Coarse	Medium	Fine	Coarse	Medium	Fine
Number of Elements	1.51M*	3.25M	6.59M	2.45M	5.28M	10.7M
C_D^A(CFD)	0.161	0.186	0.192	0.491	0.564	0.583
C_D^A(EFD) Javanmard (2013)	0.199			0.619		
Δ(%)	19.1	6.53	3.52	20.68	8.89	5.82

4.3. Mesh independence study

To ensure that the numerical solution is independent of the mesh resolution, a systematic grid refinement of $\sqrt{2}$was applied to generate three mesh configurations classified as coarse, medium, and fine with characteristics shown in Table 6 for both longitudinal and transverse modes, respectively. The drag coefficient of the underwater vehicle defined as $C_D^A = 2D/\rho V^2 A$was computed for each mesh configuration where D means drag force of the vehicle, Vrefers to the velocity ($V = 1.5$ m s^{-1}) and $A$is the projected area of the vehicle. Obtained CFD results were also compared with experimental measurements of the vehicle collected by Javanmard (2013). Clearly, the fine-mesh configurations used for longitudinal and transverse modes show the minimum relative differences of 3.52% and 5.82% with the experimental results, respectively. Therefore, using the fine-mesh configuration for each mode, guarantees that the results were mesh independent.

To confirm that mesh convergence is achieved, another mesh configuration, named as very fine grid, was generated consisting of 13.8 and 21.41 million elements for longitudinal and transverse motion modes, respectively. According to Figs. 14 and 15, using this grid configuration led to insignificant increase of 1.04% and 1.37% in predicted drag coefficient of the underwater vehicle in longitudinal and transverse motion modes, respectively. Therefore, using the fine mesh configuration for each mode ensure that the results were numerically cost effective.

Fig. 16 illustrates longitudinal cut plan on different computational grids around the vehicle including coarse, medium and fine mesh configurations. Fig. 17 illustrates the surface mesh on the vehicle. A detailed view of the computational grid corresponding to the fine-mesh configuration utilized in the mesh independence study is shown in Fig. 18.

4.4. Verification study

When adequately fine mesh resolution was generated, the capability of the CFD solver in solving the system of equations needs to be assessed. To this end, the Grid Convergence Index (GCI) method based on Richardson extrapolation method (Richardson, 1911; Richardson and Gant, 1927) was applied in this paper to estimate discretization error in CFD simulations since it is a recommended approach for estimation of discretization error in CFD simulations (Celik et al., 2008). For three mesh configurations (grid 3: course, grid 2: medium and grid 1: fine), the grid refinement factors $r_{32}$and $r_{21}$are computed as $r_{32} = h_3/h_2$and $r_{21} = h_2/h_1$where $h_i$is a representative grid size of the i^{th}grid.

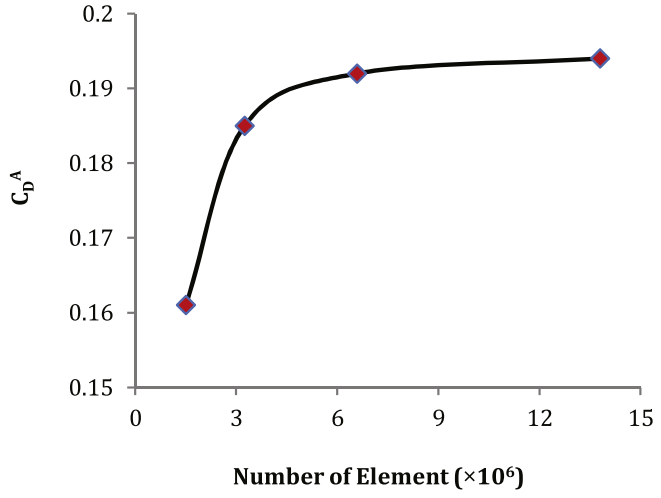

Fig. 14. Variation of the drag coefficient with the grid resolution in longitudinal motion mode.

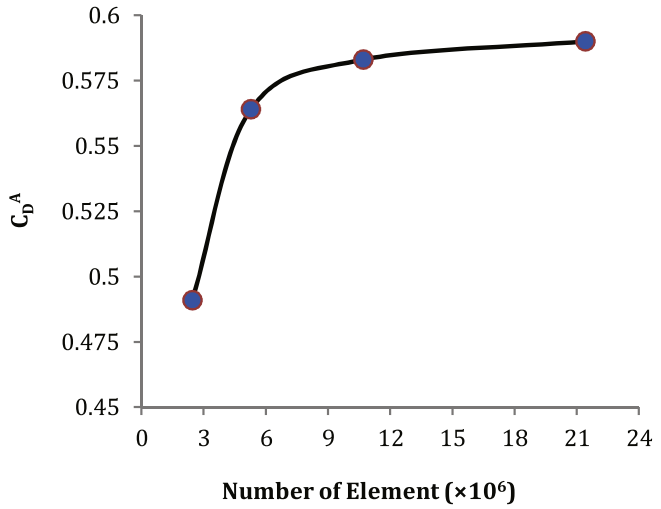

Fig. 15. Variation of the drag coefficient with the grid resolution in transverse motion mode.

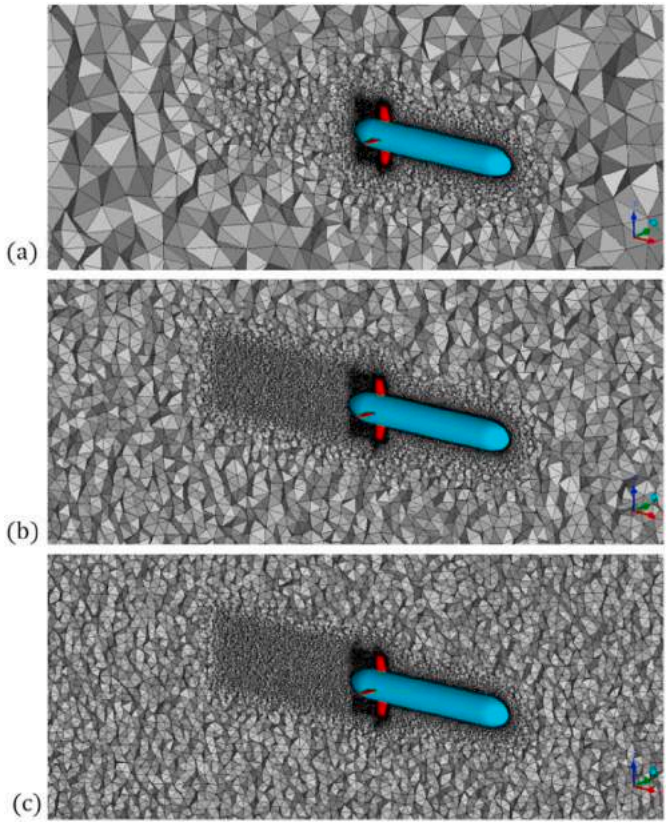

Fig. 16. Three computational grids around the vehicle generated for mesh independence study: coarse mesh (a); medium mesh (b); and the fine mesh (c).

In GCI method the first step is the calculation of the apparent order of the method, p_a, as below

$$p_a = |\ln|\varepsilon_{32}/\varepsilon_{21}| + q(p_a)|/\ln(r_{21}) \quad (33)$$

Where $\varepsilon_{32} = \varnothing_3 - \varnothing_2$and $\varepsilon_{21} = \varnothing_2 - \varnothing_1$. $\varnothing_k$is a key variable on the k^{th}grid, like C_D^Ain the present study. $q(p_a)$can be estimated as

$$q(p_a) = \ln\{(r_{21}^{p_a} - s)/(r_{32}^{p_a} - s)\} \quad (34)$$

Fig. 17. Surface mesh on the vehicle.

Where *s* can be obtained as

$$s = 1.sign(\varepsilon_{32} / \varepsilon_{21}) \tag{35}$$

The extrapolated value ($\varnothing_{ext}^{21}$), approximate relative error (e_a^{21}), and extrapolated relative error (e_{ext}^{21}) are calculated using the following equations, respectively.

$$\varnothing_{ext}^{21} = (r_{21}^{p_a}\varnothing_1 - \varnothing_2) / (r_{21}^{p_a} - 1) \tag{36}$$

$$e_a^{21} = |(\varnothing_1 - \varnothing_2) / \varnothing_1| \tag{37}$$

$$e_{ext}^{21} = \left|\left(\varnothing_{ext}^{21} - \varnothing_1\right) / \varnothing_{ext}^{21}\right| \tag{38}$$

Finally, the fine-grid convergence index is calculated by:

$$GCI_{fine}^{21} = 1.25e_a^{21} \Big/ (r_{21}^{p_a} - 1) \tag{39}$$

Table 7 presents numerical uncertainties in the estimation of the drag coefficient using three mesh configurations employed in mesh independence study. As can be seen, numerical uncertainties are around 1.23% and 1.43% for computed values of C_D^A for longitudinal and transverse motion modes, respectively. According to these values, maximum uncertainties in calculated C_D^A are ±0.0024 and ± 0.0083 for longitudinal and transverse motion modes, respectively.

5. Results and discussion

As described in section 4, two sets of velocity profiles indicated in Equations (31) and (32), have been used for CFD simulations to calculate translational added mass coefficients of the underwater vehicle in both

Table 7
Calculation of the discretization errors for C_D^A values calculated in the mesh independence study.

Parameters	Longitudinal motion mode	Transverse motion mode
r_{21}, r_{32}	$\sqrt{2}$	$\sqrt{2}$
$\varnothing_1$	0.192	0.583
$\varnothing_2$	0.186	0.564
$\varnothing_3$	0.161	0.491
p_a	4.12	3.884
$\varnothing_{ext}^{21}$	0.1939	0.5897
e_a^{21}	3.125%	3.26%
e_{ext}^{21}	0.9799%	1.136%
GCI_{fine}^{21}	1.2323%	1.434%

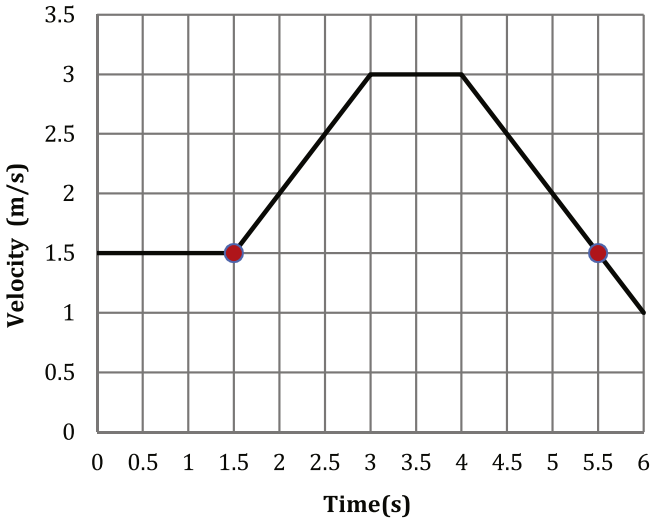

Fig. 19. Velocity profile used to simulate the accelerated motion of the vehicle in the longitudinal direction.

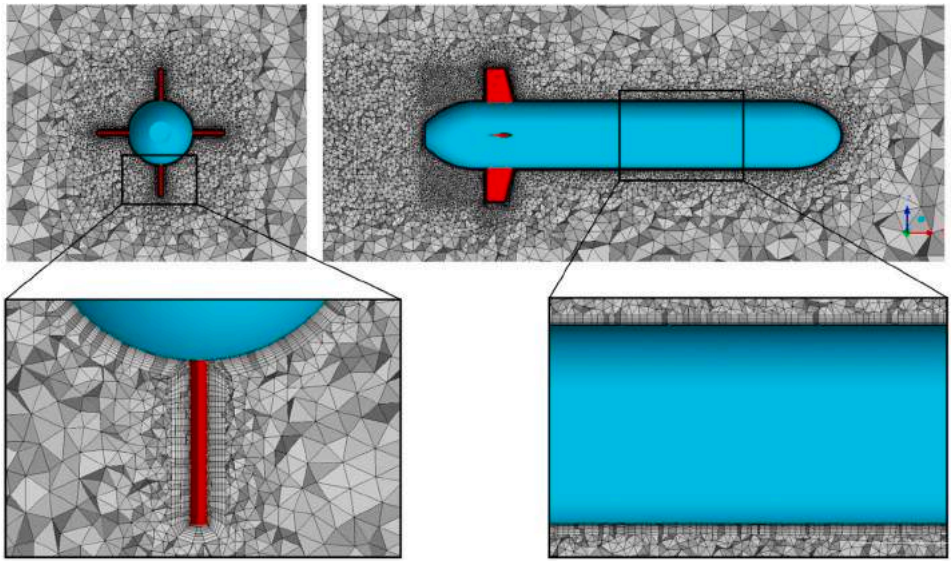

Fig. 18. Detailed views of the computational grid corresponding to the fine-mesh configuration utilized in the mesh independence study.

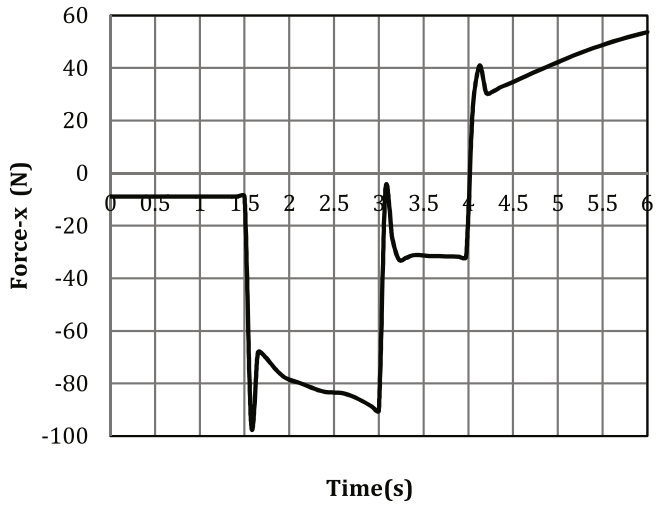

Fig. 20. Variation of the applied force on the vehicle in the longitudinal direction.

longitudinal and transverse directions ($X_{\dot{u}}$ and $Y_{\dot{v}}$). The obtained results are presented below.

5.1. Estimation of longitudinal added mass ($X_{\dot{u}}$)

The accelerated motion of the vehicle in the longitudinal direction was simulated using the velocity profile indicated in Equation (31) as shown in Fig. 19. In this case, the applied hydrodynamic force on the vehicle in the longitudinal direction is shown in Fig. 20. Using obtained hydrodynamic force in Fig. 20 and Equation (10), longitudinal added mass coefficient of the vehicle was obtained as follows:

$$X_{\dot{u}} = \frac{|F_{t=5.5} - F_{t<1.5}|}{|\dot{u}|} - \rho\forall = 3.586\ (kg) \tag{40}$$

Velocity vectors and streamlines around the rear of the vehicle at $t = 1.5$(s) and $t = 5.5$ (s)) are shown in Figs. 21 and 22, respectively. According to these figures, one can conclude that at $t = 5.5$(s) due to the deceleration of the vehicle and inertia effect of the surrounding fluid, the wake is compressed, comparing to the wake at $t = 1.5$(s). This explains how acceleration/deceleration of a vehicle creates an extra force attributed to the added mass.

In order to show that how the inertia force of the fluid surrounding the accelerating vehicle affects the hydrodynamic force applied to the vehicle, the pressure coefficient $C_P = \frac{P-P_{ref}}{\frac{1}{2}\rho U_{ref}^2}$was calculated around the vehicle at $t = 1.5$(s) and $t = 5.5$(s), as shown in Fig. 23. According to this figure, pressure distribution around the vehicle at $t = 1.5$(s) is generated due to the velocity effects that induces drag force to the vehicle whereas at $t = 5.5$(s) pressure distribution around the vehicle consists of both velocity and acceleration (added mass) effects. One can, therefore, conclude that $C_P{}^M = C_P{}^{t=5.5(s)} - C_P{}^{t=1.5(s)}$represents applied pressure to the vehicle due to added mass effects as shown in Fig. 24.

5.2. Estimation of transverse added mass ($Y_{\dot{v}}$)

The accelerated motion of the vehicle in the transverse direction was

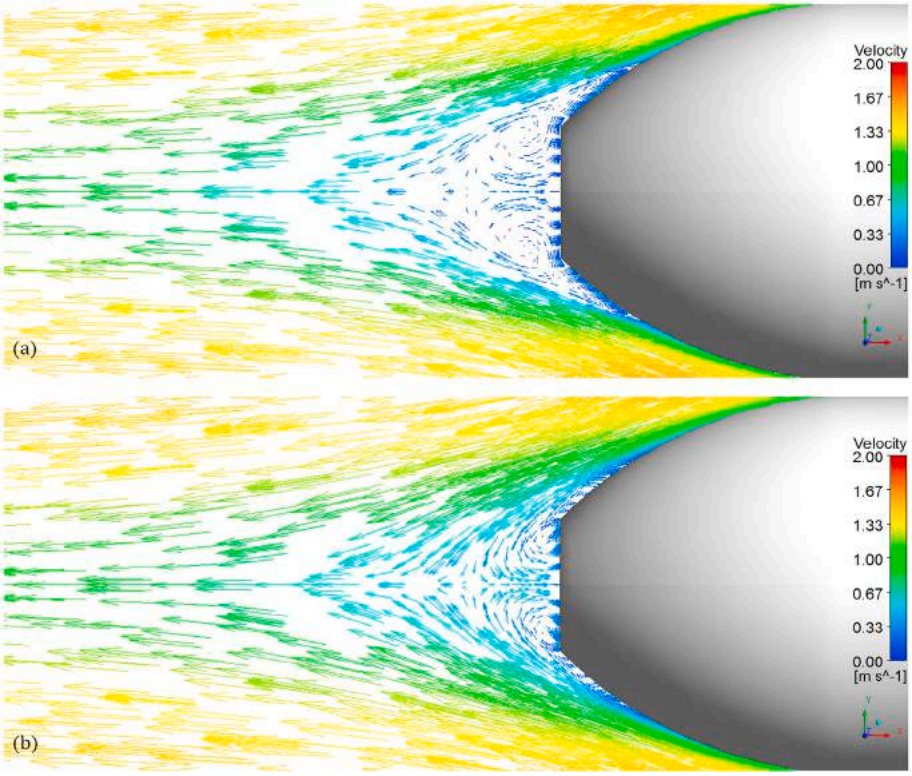

Fig. 21. Velocity vectors at the rear of the vehicle in accelerated motion in the longitudinal direction at two different times: (a) $t = 1.5$(s), (b) $t = 5.5$(s).

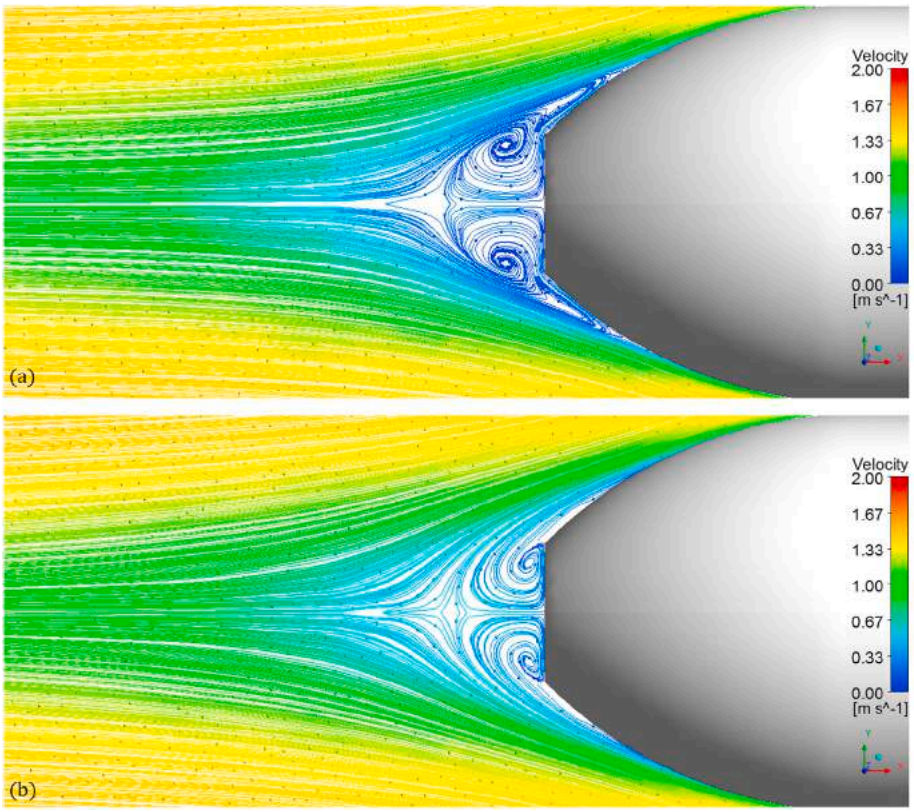

Fig. 22. Streamlines at the rear of the vehicle in accelerated motion in the longitudinal direction at two different times: (a) $t = 1.5$(s), (b) $t = 5.5$(s).

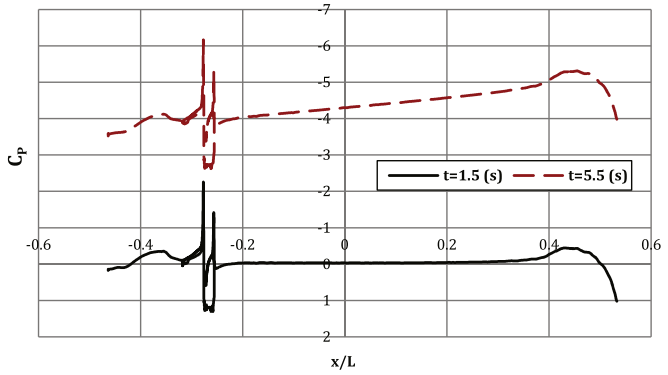

Fig. 23. Variation of the pressure coefficient (C_P) with non-dimensional parameter (x/L) around the vehicle in accelerated motion in the longitudinal direction at two different times.

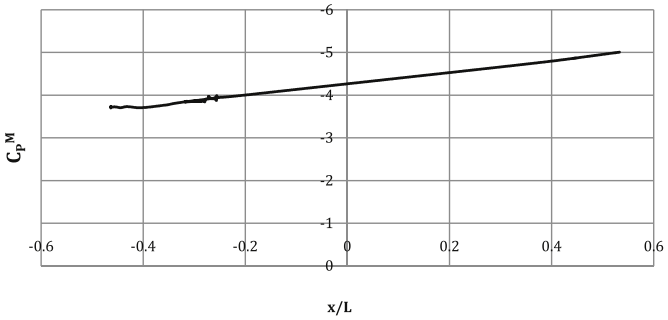

Fig. 24. Variation of the pressure coefficient applied by added mass effects ($C_P{}^M$) with non-dimensional parameter (x/L) around the vehicle in accelerated motion in the longitudinal direction at $t = 5.5$ (s).

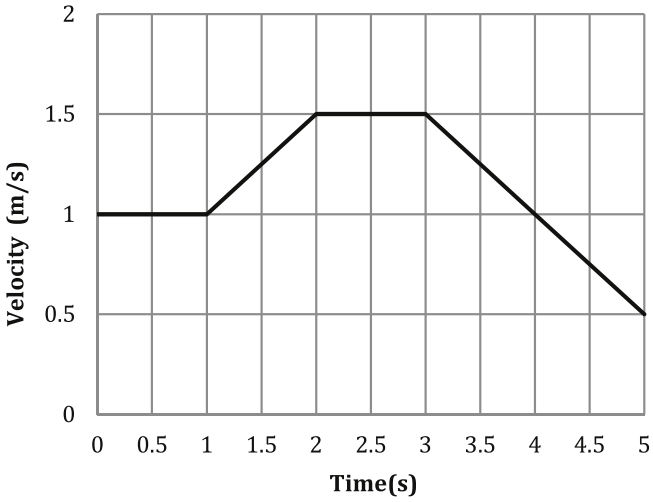

Fig. 25. Velocity profile used to simulate the accelerated motion of the vehicle in the transverse direction.

simulated using the velocity profile indicated in Equation (32) as shown in Fig. 25. In this case, the applied hydrodynamic force on the vehicle in the transverse direction is shown in Fig. 26. Using obtained hydrodynamic force in Fig. 26 and Equation (10), transverse added mass coefficient of the vehicle was obtained as follows:

$$Y_{\dot{v}} = \frac{|F_{t=4} - F_{t<1}|}{|\dot{v}|} - \rho\forall = 50.15\ (kg) \tag{41}$$

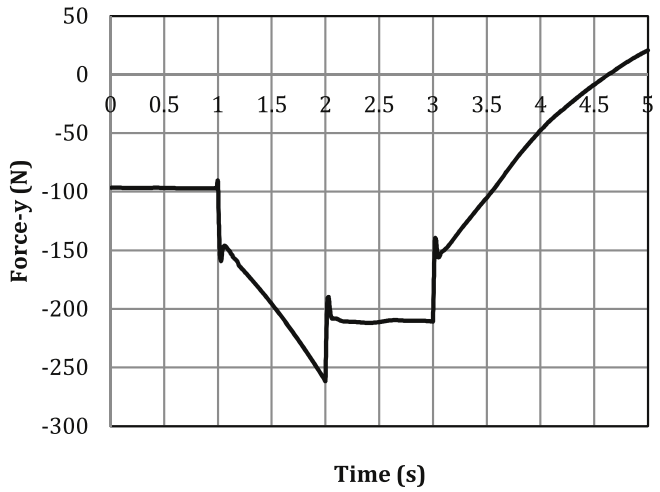

Fig. 26. Variation of the applied force on the vehicle in the transverse direction.

6. Conclusion

In the present paper, A CFD procedure was presented to calculate translational added mass coefficients of an axisymmetric underwater vehicle. To validate the obtained results, drag and added mass coefficients of an ellipsoid were obtained using the proposed CFD method and compared with the analytical and experimental results. Moreover, by performing an acceleration sensitivity study, it was shown that calculated added mass coefficients were acceleration independent. It was also shown that, the validation study revealed that the proposed CFD procedure has an acceptable level of accuracy to extract translational added mass coefficients.

A set of numerical simulations based on unsteady RANS computations was performed using ANSYS CFX software to simulate accelerated motions of the vehicle to extract translational longitudinal and transverse added mass coefficients. The proposed numerical method can be used instead of the experimental methods, which are dependent on performing oscillatory motions using PMM. The PMM are technically demanding, expensive and time-consuming with a complicated procedure in data analyzing. In addition, although applying CFD to simulate oscillatory motions in PMM tests reduces the cost of the research significantly, there are still some ambiguities in this implementation. In contrast, the presented method is not complicated and time-consuming and can be used as a reliable and inexpensive method to extract translational added mass coefficients of underwater vehicles. Moreover, the added mass coefficients obtained by the present method are more robust than the corresponding values obtained by numerical methods involving simulation of oscillating motions.

CRediT authorship contribution statement

Ehsan Javanmard: Conceptualization, Methodology, Software, Formal analysis, Investigation, Data curation, Writing - original draft. **Shahriar Mansoorzadeh:** Conceptualization, Methodology, Validation, Resources, Writing - review & editing, Supervision. **Javad A. Mehr:** Writing - review & editing.

Declaration of competing interest

The authors declare that they have no known competing financial interests or personal relationships that could have appeared to influence the work reported in this paper.

References

Aage, C., Wanger Smit, L., 1994. Hydrodynamic maneuverability data of a flatfish type AUV. In: Proceedings of the Oceans Engineering for Today's Technology and Tomorrow's Preservation, pp. 425–430. https://doi.org/10.1109/OCEANS.1994.364236. Brest, France.

ANSYS, 2009. Solver Theory Guide. Release 12.1. ANSYS Inc., USA.

Avila, J.P.J., Adamowski, J.C., 2011. Experimental evaluation of the hydrodynamic coefficients of an ROV through Morison's equation. J. Ocean Eng. 38, 2162–2170. https://doi.org/10.1016/j.oceaneng.2011.09.032.

Avila, J.P.J., Nishimoto, K., Adamowski, J.C., Sampaio, C.M., 2012. Experimental investigation of the hydrodynamic coefficients of a remotely operated vehicle using a planar motion mechanism. J. Offshore Mech. Arctic Eng. 134 https://doi.org/10.1115/1.4004952.

Barros, E.A.D., Dantas, J.L.D., Pascoal, A.M., Sa, E.D., 2008. Investigation of normal force and moment coefficients for an AUV at nonlinear angle of attack and sideslip range. IEEE J. Ocean. Eng. 33, 579–583. https://doi.org/10.1109/JOE.2008.2004761.

Bellevre, D., Diaz de Tuesta, A., Pedron, P., 2000. Submarine maneuverability assessment using computational fluid dynamic tools. In: Proceedings of 23rd Symposium of Naval Hydrodynamics. Val de Reuil, France, pp. 820–832.

Broglia, R., Mascio, A.D., Amati, G.A., 2007. Parallel unsteady RANS code for the numerical simulations of free surface flows. In: 2nd International Conference on Marine Research and Transportation (Naples, Italy).

Chen, C.W., Jiang, Y., Huang, H.C., Ji, D.X., Sun, G.Q., Yu, Z., Chen, Y., 2017. Computational fluid dynamics study of the motion stability of an autonomous underwater helicopter. J. Ocean Eng. 143, 139–227. https://doi.org/10.1016/j.oceaneng.2017.07.020.

Cimbala, J.M., 2003. A new method for calculating added mass using CFD. In: Proceedings, Division of Fluid Dynamics 56th Annual Meeting. East Rutherford, New Jersey.

Celik, I.B., Ghia, U., Roache, P.J., Freitas, C.J., Coleman, H., Raad, P.E., 2008. Procedure for estimation and reporting of uncertainty due to discretization in CFD applications. J. Fluids Eng. ASME 130. https://doi.org/10.1115/1.2960953.

Ferreira, B., Pinto, M., Matos, A., Cruz, N., 2009. Hydrodynamic modeling and motion limits of AUV MARES. In: 35th Annual Conference of IEEE Industrial Electronics, pp. 2241–2246. https://doi.org/10.1109/IECON.2009.5415198. Porto, Portugal.

Fossen, T.I., 1994. Guidance and Control of Ocean Vehicles. John Wiley and Sons.

Geisbert, J.S., 2007. Hydrodynamic Modeling for Autonomous Underwater Vehicles Using Computational and Semi-empirical Methods. MSc Thesis. Virginia Tech.

Gerfler, M., 1967. The DTMB Planar-Motion-Mechanism System. Naval Ship Research and Development Centre, Report 2528.

Go, G., Ahn, H.T., 2019. Hydrodynamic derivative determination based on CFD and motion simulation for a tow-fish. Appl. Ocean Res. 82, 191–209. https://doi.org/10.1016/j.apor.2018.10.023.

Guo, H.P., Zou, Z.J., 2017. System-based investigation on 4-DOF ship maneuvering with hydrodynamic derivatives determined by RANS simulation of captive model tests. Appl. Ocean Res. 68, 11–25. https://doi.org/10.1016/j.apor.2017.08.006.

Hopkin, D., Den Hertog, V., 1933. The hydrodynamic testing and simulation of an autonomous underwater vehicle. In: Proceedings of the Second Canadian Marine Dynamics Conference, pp. 274–281.

Hoerner, S.F., 1965. Fluid Dynamic Drag. Published by the author, USA.

Hu, Z.Q., Lin, Y., Haitao, G., 2007. On Numerical computation of viscous hydrodynamics of unmanned underwater vehicle. Robot 29, 145–150 (in Chinese).

Humphreys, D., 1981. Dynamics and hydrodynamics of ocean vehicles. In: Proceedings of IEEE OCEANS'81, pp. 88–91. https://doi.org/10.1109/OCEANS.1981.1151683. Boston, MA, USA.

Isa, K., Arshad, M.R., Ishak, S., 2014. A hybrid-driven underwater glider model, hydrodynamics estimation, and an analysis of the motion control. J. Ocean Eng. 81, 111–129. https://doi.org/10.1016/j.oceaneng.2014.02.002.

Jagadeesh, P., Murali, K., 2010. Rans predictions of free surface effects on axisymmetric underwater body. Eng. Applicat. Comput. Fluid Mechanics 4, 301–313. https://doi.org/10.1080/19942060.2010.11015318.

Jagadeesh, P., Murali, K., Idichandy, V.G., 2009. Experimental investigation of hydrodynamic force coefficients over AUV hull form. J. Ocean Eng. 36, 113–118. https://doi.org/10.1016/j.oceaneng.2008.11.008.

Javanmard, E., 2013. Determination of Hydrodynamic Coefficients of an AUV with Computational Fluid Dynamics and Experimental Fluid Dynamics Methods. MSc thesis. Department of Mechanical Engineering, Isfahan University of Technology, Isfahan, Iran.

Javanmard, E., Mansoorzadeh, S.H., 2019. A computational fluid dynamics investigation on the drag coefficient measurement of an AUV in a towing tank. J. Appl. Fluid Mech. 12, 947–959. https://doi.org/10.29252/jafm.12.03.29525.

Jones, D.A., Clarke, D.B., Brayshaw, I.B., Barillon, J.L., Anderson, B., 2002. The Calculation of Hydrodynamic Coefficients for Underwater Vehicles. Technical report DSTO Platforms Sciences Laboratory, Australia.

Kim, H., Leong, Z.Q., Ranmuthugala, D., Forrest, A., 2015a. Simulation and validation of an AUV in variable accelerations. Int. J. Offshore Polar Eng. 25, 35–44.

Kim, H., Akimoto, H., Islam, H., 2015b. Estimation of the hydrodynamic derivatives by RaNS simulation of planar motion mechanism test. J. Ocean Eng. 108, 129–139. https://doi.org/10.1016/j.oceaneng.2015.08.0.

Korvin-Kroukovsky, B.V., Jacobs, W.R., 1957. Pitching and heaving motions of a ship in regular waves. Trans. - Soc. Nav. Archit. Mar. Eng. 65, 590–621.

Korotkin, A.I., 2009. Added Masses of Ship Structures. Krylov Shipbuilding Research Institute, Springer, St. Petersburg, Russia.

Krishnankutty, P., Subramanian, V.A., Francis, R., Nair, P.P., Sudarsan, K., 2014. Experimental and numerical studies on an underwater towed body. In: Proceedings

of the ASME 33rd International Conference on Ocean. Offshore and Arctic Engineering, San Francisco, USA, pp. 8–13. https://doi.org/10.1115/OMAE2014-24400.
Lamb, S.H., 1945. Hydrodynamics, sixth ed. Dover Publications, pp. 152–155.
Lee, S.K., Joung, T.H., Cheon, S.J., Jang, T.S., Lee, J.H., 2011. Evaluation of the added mass for a spheroid-type unmanned underwater vehicle by vertical planar motion mechanism test. J. Ocean Eng. 3, 174–180. https://doi.org/10.2478/IJNAOE-2013-0060.
Leong, Z.Q., Ranmuthugala, D., Penesis, I., Nguyen, H., 2015. Rans-based CFD prediction of the hydrodynamic coefficients of DARPA SUBOFF geometry in straight-line and rotating arm manoeuvres. Trans. Royal Institution of Naval Architects Part A: Int. J. Maritime Eng. 157, A41–A51. https://doi.org/10.3940/rina.ijme.2015 al.308.
Liang, X., Li, Y., Peng, Z., Zhang, J., 2016. Nonlinear dynamics modeling and performance prediction for under actuated AUV with fins. Nonlinear Dynam. 84, 237–249. https://doi.org/10.1007/s11071-015-2442-1.
Lin, Z., Liao, S., 2011. Calculation of added mass coefficients of 3D complicated underwater bodies by FMBEM. J. Communications in Nonlinear Sci. Numerical Simul. 16, 187–194. https://doi.org/10.1016/j.cnsns.2010.02.015.
Maeda, H., Tatsuta, S., 1989. Prediction method of hydrodynamic stability derivatives of an autonomous non-tethered submerged vehicle. In: Proceedings of the Eighth International Conference on Offshore. Mechanics and Artic Engineering, Netherlands, pp. 105–114.
Malik, S.A., Guang, P., 2013. Transient numerical simulation for hydrodynamic derivatives prediction of an axisymmetric submersible vehicle. Res. J. Appl. Sci. Eng. Technol. 5, 5003–5011. https://doi.org/10.19026/rjaset.5.4388.
Mansoorzadeh, S.H., Javanmard, E., 2014. An investigation of free surface effects on drag and lift coefficients of an autonomous underwater vehicle (AUV) using computational and experimental fluid dynamics methods. J. Fluid Struct. 51, 161–171. https://doi.org/10.1016/j.jfluidstructs.2014.09.001.
Menter, F.R., 1994. Two-equation eddy-viscosity turbulence models for engineering applications. AIAA J. 32, 1598–1605.
Mishra, V., Vengadesan, S., Bhattacharyya, S.K., 2011. Translational added mass of axisymmetric underwater vehicles with forward speed using computational fluid dynamics. J. Ship Res. 55, 185–195.
Nahon, M., 1993. Determination of undersea vehicle hydrodynamics derivatives using the USAF datcom. In: Proceedings of OCEANS '93, pp. 283–288. https://doi.org/10.1109/OCEANS.1993.326107. Victoria, Canada,.
Nakamura, M., Asakawa, K., Hyakudome, T., Kishima, S., Matsuoka, H., Minami, T., 2013. Hydrodynamic coefficients and motion simulations of underwater glider for virtual mooring. IEEE J. Ocean. Eng. 38, 581–597. https://doi.org/10.1109/JOE.2012.2236152.
Pan, Y.C., Zhang, H.X., Zhou, Q.D., 2012. Numerical prediction of submarine hydrodynamic coefficients using CFD simulation. J. Hydrodynamics Ser. B 24, 840–847. https://doi.org/10.1016/S1001-6058(11)60311-9.
Park, J.Y., Kim, N., Shin, Y.K., 2017. Experimental study on hydrodynamic coefficients for high-incidence-angle maneuver of a submarine. Int. J. Naval Architecture and Ocean Eng. 9, 100–113. https://doi.org/10.1016/j.ijnaoe.2016.08.003.
Phillips, A., Furlong, M., Turnock, S.R., 2007. The use of computational fluid dynamics to determine the dynamic stability of an autonomous underwater vehicle. In: 10th Numerical Towing Tank Symposium (NuTTS'07), pp. 6–11. Hamburg, Germany.
Phillips, A., Furlong, M., Turnock, S.R., 2010. The use of computational fluid dynamics to aid cost-effective hydrodynamic design of autonomous underwater vehicles. Proc. IME M J. Eng. Marit. Environ. 239–254. https://doi.org/10.1243/14750902JEME199.
Phillips, A., Turnock, S.R., 2010. Influence of turbulence closure models on the vertical flow field around a submarine body undergoing steady drift. J. Mar. Sci. Technol. 15, 201–217. https://doi.org/10.1007/s00773-010-0090-1.
Peterson, R.S., 1980. Evaluation of Semi-empirical Methods for Predicting Linear Static and Rotary Hydrodynamic Coefficients. Technical Report. Naval Coastal Systems Center, NCSC TM-291-80.
Pook, D.A., Clarke, D.B., Jones, M., Quick, H., Ranmuthugala, D., 2018. RANS based CFD prediction of submarine hydrodynamic loads. In: 21st Australasian Fluid Mechanics Conference (Adelaide, Australia).
Prestero, T., 2001. Verification of a Six-Degree of Freedom Simulation Model for the REMUS Autonomous Underwater Vehicle. MSc thesis. Massachusetts Institute of Technology.
Rhee, K., Yoon, H.K., Sung, H.K., Kim, S.H., Kang, J.N., 2001. An experimental study on hydrodynamic coefficients of submerged body using planar motion mechanism and coning motion Device. In: International Workshop on Ship Maneuverability, pp. 1–20.
Richardson, L.F., 1911. The approximate arithmetical solution by finite difference of physical problems involving differential equations, with an application to the stresses in a masonry dam. Phil. Trans. Roy. Soc. Lond. 210, 459–470. https://doi.org/10.1098/rsta.1911.0009. Series A, Containing Papers of a Mathematical or Physical Character.
Richardson, L.F., Gant, J.A., 1927. The deferred approach to the limit. Phil. Trans. Roy. Soc. Lond. 226, 636–646. https://doi.org/10.1098/rsta.1927.0008.
Ridley, P., Fontan, J., Corke, P., 2003. Submarine dynamic modelling. In: Proceedings of the Australasian Conference on Robotics & Automation. Australian Robotics & Automation Association, Brisbane, Australia.
Saiedinezhad, A., Dehghan, A.A., Dehghan Manshadi, M., 2015. Experimental investigation of hydrodynamic characteristics of a submersible vehicle model with a non-axisymmetric nose in pitch maneuver. J. Ocean Eng. 100, 26–34. https://doi.org/10.1016/j.oceaneng.2015.03.010.
Sakamoto, N., 2009. URANS, DES Simulations of Static and Dynamic Manoeuvring for Surface Combatant. Ph.D. thesis. University of Iowa.
Sahin, I., Crane, J.W., Watson, K.P., 1993. Added mass coefficients for submerged bodies by a low-order panel method. J. Fluid Eng. 115, 452–457. https://doi.org/10.1115/1.2910159.
Sahin, I., Crane, J.W., Watson, K.P., 1997. Application of a panel method to hydrodynamics of underwater vehicles. J. Ocean Eng. 24, 501–512. https://doi.org/10.1016/S0029-8018(96)00026-1.
Sen, D.T., Vinh, T.C., 2016. Determination of added mass and inertia moment of marine ships moving in 6 degrees of freedom. Int. J. Transportation Eng. Technol. 2, 8–14. https://doi.org/10.11648/j.ijtet.20160201.12.
Shadlaghani, A., Mansoorzadeh, S.H., 2016. Calculation of linear damping coefficients by numerical simulation of steady state experiments. J. Appl. Fluid Mech. 9, 653–660. https://doi.org/10.18869/acadpub.jafm.68.225.24342.
Tang, S., Ura, T., Nakatani, T., Thornton, B., Jiang, T., 2009. Estimation of the hydrodynamic coefficients of the complex-shaped autonomous underwater vehicle TUNA-SAND. J. Mar. Sci. Technol. 14, 373–386. https://doi.org/10.1007/s00773-009-0055-4.
Tasai, F., 1969. Improvements in the theory of ship motions in longitudinal waves. In: Proceedings of the 12th International Towing Tank Conference. ITTC'69, Rome, Italy, pp. 677–688.
Tyagi, A., Sen, D., 2006. Calculation of transverse hydrodynamic coefficients using computational fluid dynamic approach. J. Ocean Eng. 33, 798–809. https://doi.org/10.1016/j.oceaneng.2005.06.004.
Wilcox, D.C., 2006. Turbulence Modeling for CFD. DCW Industries Inc., La Canada.
Wu, B.S., Fu, X., Kuang, X.F., Miao, Q.M., 2005. Investigation of hydrodynamic characteristics of submarine moving close to the sea bottom with CFD methods. J. Ship Mech. 73, 19–28.
WHITE, F.M., 1985. Fluid Mechanics, fourth ed. University of Rhode Island, Narragansett.
Zhang, H., Xu, Y.R., Cai, H.P., 2010. Using CFD software to calculate hydrodynamic coefficients. J. Mar. Sci. Appl. 9, 149–155. https://doi.org/10.1007/s11804-010-9009-9.
Zhang, X.G., Zou, Z.J., 2013. Estimation of the hydrodynamic coefficients from captive mode test results by using support vector machines. J. Ocean Eng. 73, 25–31. https://doi.org/10.1016/j.oceaneng.2013.07.007.
Zhang, S.H., Yu, J., Zhang, A., Zhang, F., 2013. Spiraling motion of underwater gliders: modeling, analysis, and experimental results. J. Ocean Eng. 60, 1–13. https://doi.org/10.1016/j.oceaneng.2012.12.023.